



ORIGINAL ARTICLE

Perfusion

Fully Automated Registration and Warping of Contrast-Enhanced First-Pass Perfusion Images

Caterina M. Gallippi,^{1,*} Christopher M. Kramer,²
Yong-Lin Hu,³ Diane A. Vido,³ Nathaniel Reichel,⁴
and Walter J. Rogers²

¹Department of Biomedical Engineering, Duke University, Durham, NC 27708

²Departments of Radiology and Medicine, University of Virginia Health System, Charlottesville, VA 22908

³Department of Medicine, Division of Cardiology, Allegheny General Hospital, Pittsburgh, PA 15212

⁴Research and Education, St. Francis Hospital, Roslyn, NY 11576

ABSTRACT

Respiratory motion during acquisition of first-pass myocardial perfusion images results in translation, distortion from out-of-plane motion, and changes in left ventricular geometry. Together these effects make visual image analysis more difficult and limit methods of quantitative analysis of contrast kinetics. We present a fully automated registration and warping algorithm for correcting translation and geometric distortions using a statistically based image registration method. Twelve patients (mean age 51 ± 12 years) were studied 3 ± 1 days after reperfused first myocardial infarction. Perfusion images were acquired during bolus administration of nonionic Gd-DTPA. Pixel intensity statistics were computed for each image in the neighborhood of high spatial frequencies. These statistics were then used to register and warp each target image (image to be registered and warped) to a common template image. Average image-to-image vertical translation was 2.6 ± 0.8 pixels (3.4 ± 1.0 mm) prior to processing and 0.9 ± 0.3 pixels (1.2 ± 0.4 mm)

*Corresponding author. Caterina M. Gallippi, Department of Biomedical Engineering, Duke University, 136 Hudson Hall, Box 90281, Durham, NC 27708. Fax: (919) 684-4488; E-mail: caterina.gallippi@duke.edu

post-processing ($P < 0.0001$). Mean image-to-image horizontal translation was 1.7 ± 1.2 pixels (1.8 ± 1.2 mm) before and 1.3 ± 0.7 pixels (1.4 ± 0.7 mm) after processing ($P = 0.05$). Left ventricular endocardial area varied an average of 105 ± 55 pixels (140.7 ± 53.7 mm²) between images prior to processing vs. 51 ± 15 pixels (68.3 ± 20.1 mm²) after processing ($P < 0.001$). Thus automated, statistically based registration and warping of perfusion images is effective in reducing image-to-image translation. This method may permit more sensitive qualitative and quantitative evaluation of myocardial contrast-enhanced first-pass images.

Key Words: Magnetic resonance; Myocardial perfusion; Image processing; Image registration

INTRODUCTION

First-pass myocardial perfusion using T1 shortening agents is useful in identifying regions of ischemia and necrosis.^[1-5] The time required to image first-pass transit and early equilibrium of the contrast material precludes imaging during a single breath hold. Respiration causes the heart to move within and through the image plane, and variations in cardiac cycle length result in changes in cardiac geometry including wall thickness. Together these changes limit quantification of perfusion parameters and make qualitative evaluation more difficult, reducing routine clinical application. MRI perfusion provides sufficient spatial resolution to evaluate the transmural extent of first-pass defects. However, due to respiratory-related cardiac motion, quantitative analysis is generally reduced to a limited number of manually positioned regions of interest (ROI). Previous analysis of myocardial contrast agent kinetics has included perfusion reserve index,^[6] maximal uptake slope, time-to-peak signal intensity, mean transit time,^[7] and the contrast transfer constant.^[8] These methods show promise as a means of improving the sensitivity for the detection of subtle perfusion defects, which may not be appreciated by visual inspection. A number of approaches have been applied to registration and warping of perfusion images.^[9-13] These require significant operator interaction or can only be applied to LV short-axis images. The present study presents a fully automated method of combined image registration and warping based on matching regions of highly variable pixel intensities. Given that the method does not track specific shapes or features, it is independent of acquired cardiac orientation.

METHODS

Patient Population

Twelve patients (mean age 51 ± 12 years) were studied 3 ± 1 days after reperfused first myocardial infarction (MI). Table 1 shows the clinical parameters.

Image Acquisition

Images were acquired on a 1.5T Siemens Vision scanner (Erlangen, Germany) using a phased array chest coil. Perfusion images were acquired using an inversion prepared T1-weighted TurboFLASH technique. Based on location of the MI, two left ventricular short-axis slices (apex, mid, or base) and one long-axis (2- or 4-

Table 1

Clinical Variables

Variable	
Age	51 ± 12 years
Gender	10 (83.3%) male
Peak CK	3237 ± 2586
EF	$45 \pm 11\%$
MI location	
Anterior	7 (58%)
Posterior	1 (8%)
Inferior	4 (33%)
Days to MRI	3 ± 1 days
Time to refer	372 ± 263 min
Stent	8 (67%)
Lytics	2 (17%)

chamber) images were acquired during each cardiac cycle. Parameters included: TR = 3.7 msec, TE = 1.2 msec, field of view = $263 \times 330 \text{ mm}^2$, matrix 80×128 phase and frequency lines, $3.2 \times 2.7 \text{ mm}^2$ pixels, 10 mm slice thickness. Images were interpolated to 256×256 prior to processing yielding a calibration of $1.0 \times 1.3 \text{ mm}^2/\text{pixel}$. Time-intensity (TI) was adjusted based on RR interval to maximally suppress myocardial signal prior to contrast infusion. Gd-DTPA (Magnevist, Berlex, Wayne, NJ) at a dose of 0.1 mM/kg was injected at a rate of 5 mL/sec using a Medrad Spectris MR compatible power injector (Indianola, PA). Images were acquired over 50 heart cycles during normal breathing.

Image Processing

Images were transferred to a Sun Ultra Sparc workstation (Mountainview, CA) for processing. A single image in the center of the acquisition period demonstrating good myocardial to cavity contrast was defined as the template image for each LV location. The center image was designated as the template because it was likely to be the most similar to all the other images in the data set. Scout images used to define the LV short and long axes insured that the heart was centered in the image matrix. Processing was limited to a 128×128 region that included the heart and excluded chest wall and other remote noncardiac structures. The present approach registers and warps first-pass images at a given location to the location-specific template image. For each pixel in the template image, the local intensity variation extent, mean, and standard deviation in an 11×11 pixel ($11.3 \times 14.3 \text{ mm}^2$) window around the pixel of interest were computed. As defined by Wu and Murani^[14] the local intensity variation extent is

$$\text{Var} = 1 - \frac{1}{(1 + \alpha_1 \delta_w)} \quad (1)$$

where α_1 is a constant that depends on the input images' histograms and δ_w is the standard deviation within the 11×11 window. The size of the window was determined empirically to be large enough to represent the expected local information but small enough to avoid blurring the statistical distribution in the region surrounding the pixel of interest. Finally, the direction of increasing pixel intensity, or the edge direction, for each template pixel was determined as described below. For pixel p_{ij} ,

$$\text{edge}_h = \text{sign}[(p_{i+1,j-1} + 2p_{i+1,j} + p_{i+1,j+1}) - (p_{i-1,j-1} + 2p_{i-1,j} + p_{i-1,j+1})] \quad (2)$$

$$\text{edge}_v = \text{sign}[(p_{i-1,j+1} + 2p_{i,j+1} + p_{i+1,j+1}) - (p_{i-1,j-1} + 2p_{i,j-1} + p_{i+1,j-1})] \quad (3)$$

where edge_h is the horizontal edge direction and edge_v is the vertical edge direction.

Prior to registration, each target image was convolved with a 3×3 nonlinear Sobel edge enhancement filter (IDL, Research Systems, Boulder, CO). The edge detected version of the target image was partitioned into 16 blocks, and pixels on the strongest 20% of the edges in *each* block were automatically designated as "landmark" pixels. There needed to be enough blocks to guarantee a distribution of landmarks throughout the target image but not too many blocks such that weak edges were designated as landmark pixels. Further, the criterion that only the strongest 20% of edges became landmark pixels ensured that landmarks were located in regions of relative high spatial frequency. For each landmark pixel in the target image, the local intensity variation extent, mean, and standard deviation were computed in the 11×11 kernel, and the edge direction was found as described in Eqs. (1)–(3) for the template image. Figure 1a–c shows an example of unprocessed short-axis image, the same image after application of a Sobel filter, and after identification of the landmark pixels in 16 sectors, respectively.

For each landmark pixel in the target image, the best matching pixel in a 21×21 pixel ($21.6 \times 27.3 \text{ mm}^2$) search window in the template image was identified. The search window size was chosen empirically to be large enough to accommodate anticipated motion but small enough to keep computational cost within reason. The quality of the match was quantified by calculating a score that is a function of the previously calculated local intensity variation extents, means, variances, and edge directions as follows:

$$\text{Score} = \frac{(I_1 - I_1^{\text{ave}})}{\sqrt{\alpha^2(I_1)\alpha^2(I_2)}} \times \text{Var}_1 \times \text{Var}_2 \times \{(\text{edge}_{v1} \times \text{edge}_{v2}) \times (\text{edge}_{h1} \times \text{edge}_{h2})\} \quad (4)$$

where I represents pixel intensity, I^{ave} is the mean intensity, Var is the computed local intensity variation extent, edge_v is the vertical edge direction, and edge_h is the horizontal edge direction. The number "1" corresponds to the target image and the number "2" signifies the template image. Using this criterion for matching pixels, each landmark pixel was individually assigned a unique translation corresponding to the index of the respective highest scoring pixel in the template image.

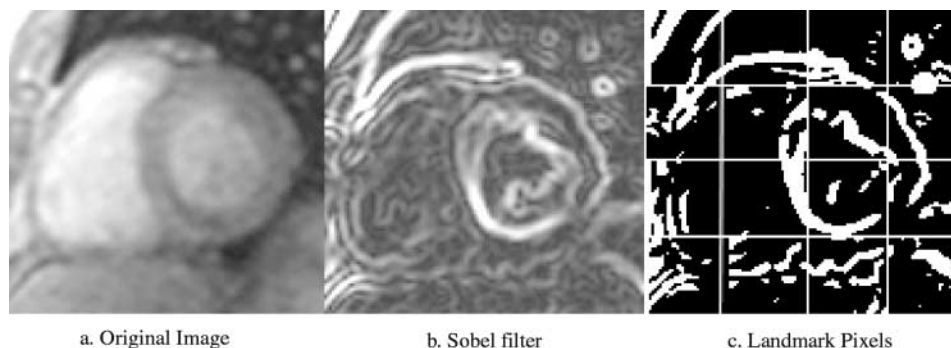


Figure 1. Unprocessed LV short-axis image after first-pass of contrast agent through myocardium (a). Image after filtering with Sobel edge enhancement filter (b). After dividing image matrix into 16 equal sections, landmark pixels are identified as top 20% of signal intensity in each sector (c).

The registration was not necessarily rigid; each landmark pixel could have been translated independently of any other pixel.

After every landmark pixel in the target image was matched to a template image pixel, the predicted translations were used as input to warp the target image to the template image. The warping routine employed was “warp-tri” in IDL (Research Systems, Boulder, CO). This process was repeated for all other target images at different time points. In summary, the described technique performs fully automated registration and warping via the following steps:

1. Select an image in the center of the data set as the template image.
2. Compute statistical information and edge directions for every template pixel.
3. For each target image,
 - a. Perform edge detection.
 - b. Automatically designate landmark pixels.
 - c. Compute statistical information and edge directions for every landmark pixel in the target image.
 - d. Search for each landmark pixel’s best matching pixel in the template search kernel with Eq. (4).
 - e. Warp the target image to the template using the computed pixel translations.
4. Repeat step 3 for all target images.

Validation Using Synthetic Images

The presented registration and warping algorithm was validated with sets of three sample time series synthetic images created in a 256×256 , 8-bit matrix. All series

were tested with various amounts of uniformly distributed random noise achieving 27, 17, and 13 dB signal-to-noise ratios (SNRs). The first series of test images examined the algorithm’s robustness for detecting geometric variability. Three rings centered at image pixel co-ordinate (128, 128) where (0, 0) corresponds to the top left portion of the image matrix with increasing diameters of 15, 20, and 22 pixels, respectively, were processed. The first and third images were registered and warped to match the center image. The test was repeated for each SNR level. The second series of validation images tested the ability of the registration algorithm to correct for rigid-body translation. Three identical rings were initially centered at (128, 128), (133, 133), and (135, 135). The first and third images were warped to the center “template” image. The test was repeated for each SNR level. In order to confirm that the algorithm operated without any dependence on object shape, the translation was repeated using a shifting diagonal bar with a long-axis dimension of 30 pixels and a short-axis dimension of 10 pixels. The bar was shifted 5 pixels horizontally between the first and second image and 2 pixels between the second and third images. Again the center image was used as the template. Figure 2 shows representative examples of simulated images.

Image Analysis

After processing, horizontal and vertical translation (corresponding to left–right and anterior–posterior anatomic directions) were compared between raw and processed images by determining the center-of-area of manually drawn LV epicardial contours at each time point (NIH Image 1.61) as described previously by Fogel et al.^[15] Image-to-image change in myocardial area was

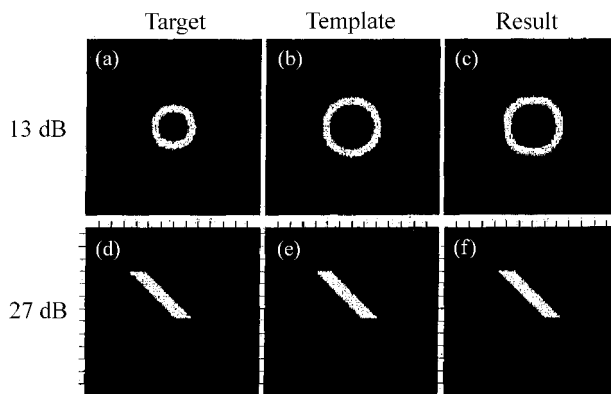


Figure 2. Computer-generated images of a ring with 13 dB SNR and bar with a 27 dB SNR. The images in the leftmost column are the images to be translated and warped to match the corresponding “template” images in the center column. The target ring has an outer diameter of 15 pixels while the template ring has a diameter of 20 pixels. The target bar is translated 5 pixels to the left of the template. The rightmost column shows the appearance of the warped and translated ring (top) and bar (bottom).

determined by manually positioning an additional LV endocardial contour and determining image-to-image and accumulated change in both epicardial and endocardial area. The effect of LV translation, change in geometry, and the impact of the present processing method were evaluated using eight circular, 6 mm diameter, evenly spaced, ROI positioned within the LV wall. Time-intensity curves were generated for each ROI in raw and processed image sets.

Parametric Images

We have previously used parametric maps to visualize myocardial perfusion kinetics.^[16] Smooth TI curves are generated for each pixel location across the 50 acquired inversion prepared T1 weighted images during myocardial transit of Gd-DTPA. Parametric maps were generated by recording the parameter of interest in each pixel location. Seven parameters were calculated. Values were scaled to fit an 8-bit, 0–255 gray scale. *Peak signal intensity* across time identifies regions of persistent hypoenhancement. *Time-to-peak signal* maps the flow-related early period of enhancement. Bright regions indicated delayed early myocardial enhancement. *Maximum upslope* is used to map the rate of early signal enhancement. *Time-to-maximum upslope* identifies regional differences in the time required to reach the maximum “rate” of signal enhancement. The *backward*

slope displays the regional rate of signal decline associated with early contrast “wash-out,” and *backward slope time* displays the time required to reach peak “wash out.” Finally, the *signal intensity range* for each pixel indicates the relative extent of myocardial signal enhancement. Parametric maps were generated using raw and processed image data in one normal volunteer and two patients following myocardial infarction.

Statistical Analysis

Results for pooled data including clinical variables, left ventricular centroid translations before and after processing, and change in left ventricular epicardial area before and after processing are expressed as mean \pm standard deviation. Methods of image analysis such as parametric analysis can be measured in pixel units, therefore results are expressed in pixels. Paired *t*-tests were used to compare displacement and area between raw and processed data. In cases where the paired data was not normally distributed, Wilcoxon’s signed-rank test was used. All tests of significance are 2-tailed. *P*-values < 0.05 were considered significant. Analysis of variance was used to determine if translation varied by location or orientation.

RESULTS

Validation Using Simulated Images

Figure 2 displays examples of computer-generated images used to validate the accuracy of the warping and registration algorithm. Figure 2a is a ring with a 15-pixel diameter that was warped to match Fig. 2b, a ring with a 20-pixel diameter. The resulting ring is shown in Fig. 2c. Figure 2d and e shows images of diagonal bars misaligned in the horizontal direction by 5 pixels. Figure 2f shows that the shape of the bar was undistorted after the algorithm translated 2d to the position of the bar in Fig. 2e. Tables 2 and 3 show the results of computer simulations to test the algorithm’s ability to correct for (1) change in object geometry (expanding ring), (2) rigid body translation (translating ring), (3) rigid body translation (translating diagonal bar), and (4) differing levels of background noise (range of SNR).

NIH Image 1.61 was employed to assess the algorithm’s performance with the validation images. In the case of the expanding rings, geometric area was determined by fitting a circular contour to the outer border of each ring and integrating the number of encompassed pixels. Position and translation was

Table 2
Registration and Warping of Rings with Different Diameters and Noise Levels

Frame #	Actual Ring Area (Pixels)	Observed Area 13 dB (Pixels)	Observed Area 17 dB (Pixels)	Observed Area 27 dB (Pixels)
1	706.8	1295.1	1294.7	1290.0
2	1256.6 (template)	1256.6	1256.6	1256.6
3	1520.5	1307.1	1295.2	1287.9

determined by computing the center-of-area of the same contour. Ring areas prior to processing were 706.8, 1256.6, and 1520.5 pixels, respectively, with the center ring serving as the template image. After processing, the mean area of the smallest ring, pooled over the three noise levels was 1293.3 ± 2.8 pixels, 2.9% greater than the template. The mean area of the largest ring after processing was 1296.7 ± 9.9 pixels, 3.2% greater than the template. There was a trend toward greater area overestimation in the presence of greater noise (13 vs. 27 dB).

Table 3 displays results for correction of translation in ring and bar shapes. Prior to processing, the center-of-area of rings in the 256×256 pixels images was (128, 128) for the first image, (133, 133) for the center "template" image, and (135, 135) for the third simulated image. After processing, the average center-of-area pooled over noise levels was $(133.1 \pm 0.7, 132.3 \pm 0.4)$ for the first image and $(132.2 \pm 1.1, 133.2 \pm 0.5)$ for the third image. The center-of-area for the bar prior to processing was (120, 114) for the first image, (125, 114) for the center "template" image, and (126, 114) for the third image. After processing, the mean center-of-area for the bar was $(125.4 \pm 0.3, 114.5 \pm 0.3)$ and $(125.6 \pm 0.7, 114.5 \pm 0.4)$ for the first and third images, respectively. The information presented in Table 3 is displayed graphically in Fig. 3.

After verifying the registration and warping methods with synthetic images, clinical images were registered

and warped. Prior to processing, horizontal translation in the short axis, 2- and 4-chamber long axis was 1.9 ± 1.4 , 1.6 ± 1.2 , and 1.0 ± 0.6 pixels, respectively (ANOVA, $P = \text{NS}$). This corresponded to left-right, anterior-posterior, and left-right displacements, respectively. After registration and warping, vertical translation in these orientations was 1.4 ± 0.7 , 1.3 ± 0.6 , and 1.3 ± 0.7 pixels, respectively (ANOVA, $P = \text{NS}$), corresponding to anterior-posterior, superior-inferior, and anterior-posterior, respectively. Vertical translation in the short axis, 2- and 4-chamber orientation prior to processing was 2.3 ± 0.8 , 2.5 ± 0.8 , and 2.4 ± 1.5 pixels (ANOVA, $P = \text{NS}$). Processed data in these orientations (1.1 ± 0.7 , 1.0 ± 0.38 , and 1.1 ± 0.23 pixels, respectively) were not different between orientations (ANOVA, $P = \text{NS}$). Left ventricular translations prior to and after processing were not different based on orientation, and therefore, results are pooled. Results shown in Table 4 indicate that prior to corrective image processing mean image-to-image LV translation was greater in the vertical direction (2.5 ± 0.8 pixels) than in the horizontal direction (1.6 ± 1.1 pixels, $P < 0.03$). Accumulated LV translation ("cumulative displacement") was also greater in the vertical direction (61.6 ± 20.2 pixels) than in the horizontal direction (39.9 ± 27.5 pixels) over the 50 acquired perfusion images. After processing, average horizontal and vertical translation was reduced to 1.2 ± 0.6 and 1.0 ± 0.5 pixels, respectively. This was a significant decrease in

Table 3
Registration of Simulated Images with Known Translation

	Actual Position			Observed Position (13 dB)			Observed Position (17 dB)			Observed Position (27 dB)		
Ring	128x	133x	135x	132.4x	133x	131.2x	133.3x	133x	133.3x	133.7x	133x	132.9x
	128y	133y	135y	131.8y	133y	133.7y	132.5y	133y	132.9y	132.5y	133y	132.9y
Bar	120x	125x	126x	125.6x	125x	126.2x	125.4x	125x	125.6x	125.1x	125x	124.9x
	114y	114y	114y	114.3y	114.0y	114.6y	114.5y	114y	114.8y	114.8y	114y	114.1y

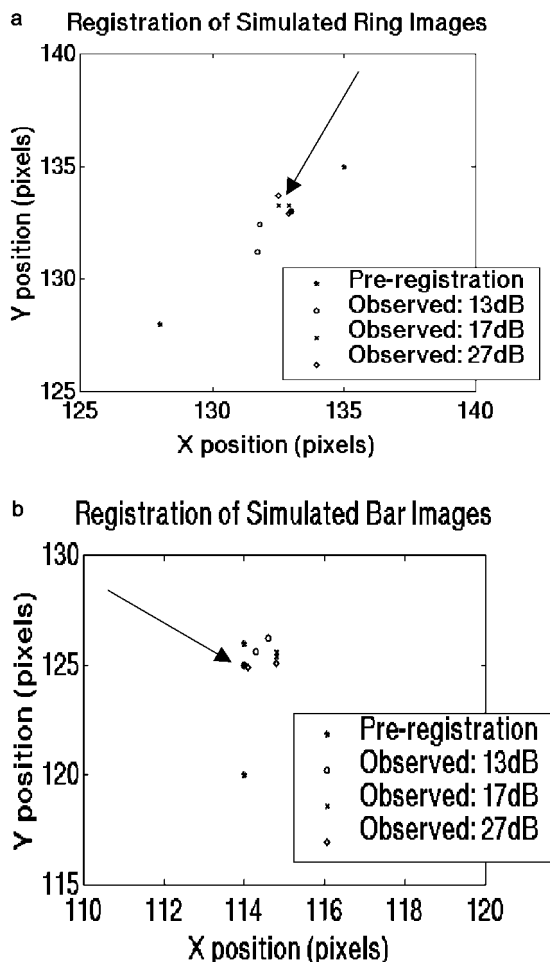


Figure 3. Central location in pixels of synthetic ring (a) and bar (b) images prior to registration (*) and post-registration for 13 dB (○), 17 dB (×), and 27 dB (◇) SNR images. The central location of the template image is demarked with an arrow.

both directions ($P < 0.03$ and $P < 0.0001$, respectively). After processing, there was little difference in mean horizontal and vertical translation. Accumulated horizontal and vertical translation over the imaging period was significantly reduced to 29.1 ± 15.8 ($P < 0.03$) and 26.7 ± 13.8 ($P < 0.0001$), respectively. These results are reflected in the individual patient data shown in Fig. 4a (left–right translation) and b (anterior–posterior translation). Data points in graphs have been normalized to the first time-point. Due to the greater translation in the anterior–posterior direction, the effect of processing is more apparent in Fig. 4b. The periodicity of the raw data reflects the patient’s breathing pattern.

Table 5 displays the image-to-image change in endocardial and epicardial area as well as the accumulated area change during the acquisition period. Average epicardial area was 2317 ± 619 pixels ($3104.8 \pm 829.5 \text{ mm}^2$) while endocardial area averaged 1037 ± 526 pixels ($1389.6 \pm 704.8 \text{ mm}^2$). Image warping had little effect on change in image-to-image epicardial area, which averaged 101 ± 43 pixels ($135.3 \pm 57.6 \text{ mm}^2$) before and 103 ± 29 pixels ($138.0 \pm 38.9 \text{ mm}^2$) after processing. This represents a 4.4% change in epicardial area for both pre- and post-processed data. However, average endocardial area change was reduced from 105 ± 55 pixels ($140.7 \pm 73.7 \text{ mm}^2$) to 51 ± 15 pixels ($68.3 \pm 20.1 \text{ mm}^2$) after processing, which represents a percentage decrease from 10.1 ± 8.1 to $4.9 \pm 2.9\%$, respectively ($P < 0.001$).

Time–intensity curves based on ROI placed within the myocardial wall are sensitive to both translation and changes in geometry. Figure 5 compares TI curves between raw and processed data at an anterior mid short-axis location. Oscillations seen in the raw data are reduced in the processed data.

Table 4

Effect of Registration and Warping on Left Ventricular Misalignment^a

	Mean Horizontal Displacement (Pixels)	Mean Vertical Displacement (Pixels)	Cumulative Horizontal Displacement (Pixels)	Cumulative Vertical Displacement (Pixels)
Raw	1.6 ± 1.1^b	2.5 ± 0.8	39.9 ± 27.5^b	61.6 ± 20.3
Processed	1.2 ± 0.6	1.0 ± 0.5	29.1 ± 15.8	26.7 ± 13.8
P-value	0.03	< 0.0001	0.03	< 0.0001

^aLeft ventricular displacement (pixels).

^b $P < 0.03$ vs. corresponding y-value.

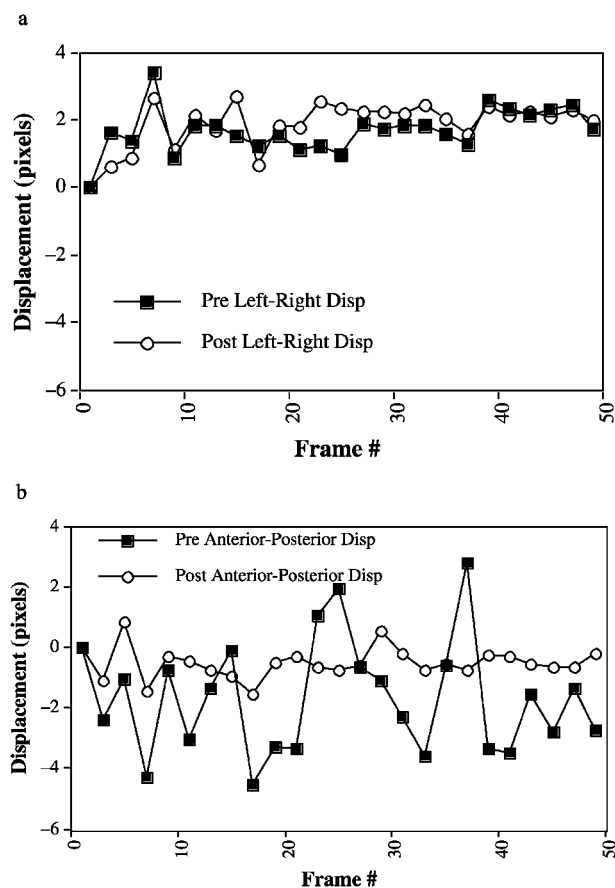


Figure 4. Short-axis LV displacement in the left–right direction (a), normalized to the original pixel position, is shown for a sample patient. Original data is identified by filled squares, processed data by open circles. The x -axis indicates displacement for every other time point in the 50-image perfusion acquisition. Anterior–posterior displacement of the LV (b) for the same patient is more exaggerated prior to processing. After processing displacements in the two directions are similar.

Figure 6a–l compares parametric maps generated from 50 raw and processed images in a normal volunteer acquired in the 4-chamber long-axis orientation. Regional signal intensity variation in the peak signal intensity maps Fig. 6a and b are similar between raw and processed data sets. However, in the time-to-peak map, translation in the unregistered images produces an artifact (arrow, Fig. 6c) seen as a region of enhanced intensity along the endocardial border of the left ventricular septum. This artifact is absent in the map generated from registered images (Fig. 6d). In general, the regional distribution of signal intensity compared well between maps generated from raw vs. processed images. The effect of uncorrected translation resulted in artifacts along the septum in time-to-maximum upslope (arrow, Fig. 6g), and time to maximum downslope (Fig. 6k).

Figure 7a–l shows the effect of translation in images acquired in the short-axis orientation in a patient with an inferior subendocardial MI. A region of persistent hypoenhancement is well seen in the peak signal intensity map generated from processed images (Fig. 7b) but is less obvious in the map generated from unregistered images (Fig. 7a). This defect is also better defined in maps generated from registered data displaying maximum upslope (arrow, (Fig. 7f) and maximum downslope (Fig. 7j).

Figure 8a–l displays maps generated from a set of basal short axis images in a patient following a basal lateral subendocardial MI. A region of persistent hypoenhancement is documented on the peak signal intensity maps (Fig. 8a and b). While maps generated from either registered or unregistered images display abnormal patterns, the subendocardial nature of the perfusion abnormality is better appreciated in maps from processed images.

Table 5

Change in Left Ventricular Area (pixels)

	Mean Endo Area Change (Pixels)	Mean Epi Area Change (Pixels)	Cumulative Endo Area Change (Pixels)	Cumulative Epi Area Change (Pixels)
Raw	105 ± 55	101 ± 42	2619 ± 1362	2526 ± 1063
Processed	51 ± 15	103 ± 29	1453 ± 390	2581 ± 733
<i>P</i> -value	<i>P</i> < 0.001	NS	<i>P</i> < 0.01	NS

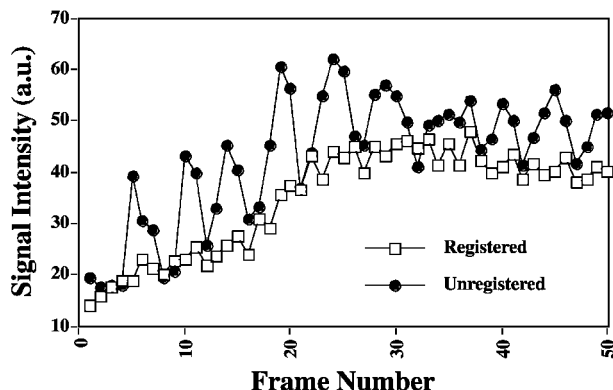


Figure 5. Time-intensity graphs are compared in an ROI positioned in the anterior LV location within a short-axis image series. Oscillations due to respiratory induced LV translation are seen in the raw image set (●), but are reduced after image processing (□).

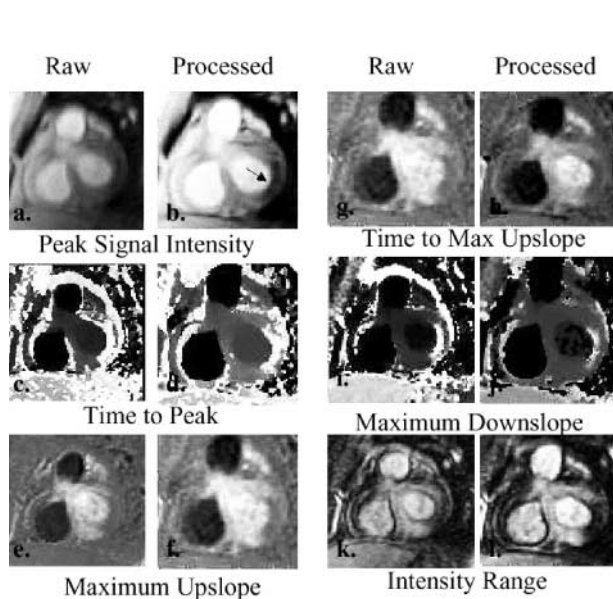


Figure 6. Comparison of parametric maps in a normal volunteer (4-chamber orientation) between raw inversion-recovery prepared perfusion images and images which have been registered and warped. Peak signal intensity (a, b), and maximum upslope (e, f) maps show similar uniform signal within the left ventricular wall. Time-to-peak signal maps show the effect of uncorrected inter-phase image translation. While the signal in the processed image is uniform (d) there is an artifactual line of signal increase (arrow, c) along the endocardial LV septum. A similar artifact is seen in (g) in the basal septum (arrow) and along the entire endocardial septum in the time to maximum downslope (k).

DISCUSSION

Contrast-enhanced MR myocardial perfusion imaging offers the potential to quantify nontransmural first-pass perfusion defects. Further, analysis of contrast kinetics on a pixel-by-pixel basis may increase the sensitivity beyond that obtained using visual inspection alone. The present approach uses image intensity statistics to automatically generate landmark pixels in 16 sectors within a region of the myocardium. Dromigny-Badin et al.^[10] manually identified landmarks within MR cine and MR perfusion images in order to perform affine transformation of the two image sets. Their approach is attractive in that it is independent of orientation. It is effective on LV long axis as well as on LV short axis images. The described method is also independent of orientation, and automatic landmark detection gives the presented method a significant advantage over techniques that require operator-identified landmarks. Also, the presented registration method is

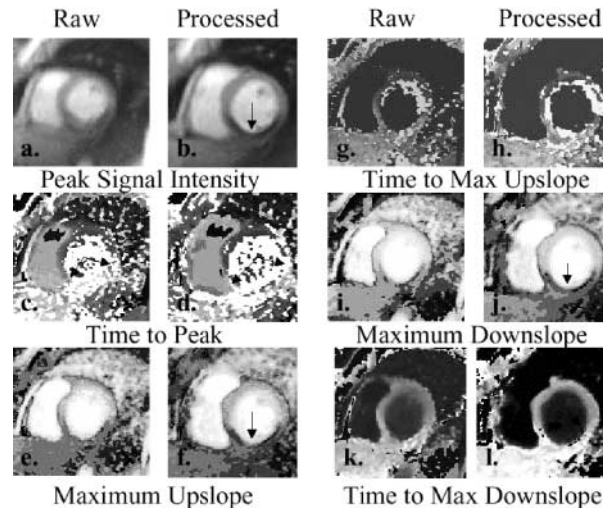


Figure 7. Parametric maps calculated from short-axis inversion-recovery prepared perfusion images in a patient following an inferior MI. The peak signal intensity map generated from registered images shows a clear inferior subendocardial region of persistent hypoperfusion (arrow, b). Failure to correct for image-to-image translation results in blurring and loss of contrast as seen in the map from the raw data (a). The subendocardial extent of this patient's perfusion defect is shown in the maximum upslope and downslope maps (f, j) from registered images but is less obvious in maps from unregistered images. The time-to-maximum downslope, a measure of contrast washout, is seen to be delayed (brighter) for the entire inferior region (between arrows, l), while the corresponding map from unregistered images shows less contrast between the inferior and remote anterior LV wall.

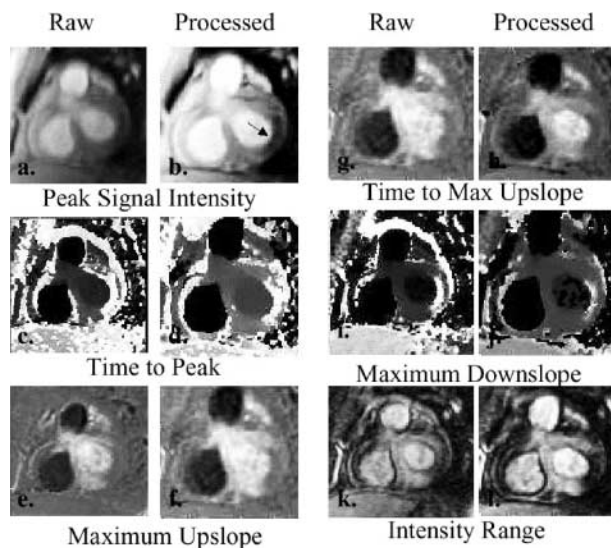


Figure 8. Parametric maps from basal short-axis saturation-recovery prepared perfusion images in a patient following a basal-lateral MI. A region of persistent hypoenhancement is seen in (b) (arrow) but is not well seen in the map using unregistered images (a). Time-to-peak (c, d) and maximum upslope maps (e, f) are similar between maps from raw or processed images. Time-to-maximum upslope maps show a clear defect in 8h, not well seen on (g). The same is true for observed defects in maximum downslope maps (i, j). When mapping for the signal intensity range seen across the perfusion image phases, the “range” map generated from processed data shows a clear transmural gradient of signal intensity, corresponding to the ischemic wavefront not seen on the map from raw data.

performed on a pixel-by-pixel basis, so the technique is not limited to affine transformations.

Automatic landmark detection has been proposed previously by Becker et al.^[17] in order to perform real-time retinal tracking. Becker et al. reliably identified vascular branching and used those locations as landmark points. The present method does not rely on the presence of specific anatomical features such as vessel branching. Instead, any general pixel in an area of high-frequency image information is automatically identified as a landmark. Becker et al. matched landmark local edge direction histograms to improve matching between landmarks in multiple images. The present method only compares the horizontal and vertical edge direction associated with each pixel and therefore incurs comparatively lower computational expense.

Translation and deformation tracking of MR perfusion images has been described previously by Yang et al.^[9] In

distinction to the present method, Yang registered LV short-axis images using phase information contained in the raw MR image data. Their investigation, along with the present study, reported greater vertical than horizontal LV displacement in short-axis perfusion images. Changes in the epicardial and endocardial borders occurring across time were tracked after images were transformed to the polar co-ordinate system. Contours were then modified to be congruent with the local LV wall structure. This approach may be less applicable to short-axis images from hearts geometrically deformed post-infarction or to other standard orientations such as the 2- and 4-chamber long-axis views. The present method is independent of acquired cardiac orientation.

As with other 2D registration and warping methods, our technique does not correct for through-plane motion. During free breathing, Danias et al.^[18] observed an average of 9 ± 3 mm superior-inferior motion of the left main coronary artery. Systolic excursion of the LV base toward the apex is an additional cause of through plane motion. We previously reported total motion throughout the cardiac cycle to average 15 mm at the LV base and less than 2 mm near the apex.^[19] Perfusion images acquired at a single point in the cardiac cycle would represent significantly less contraction related through-plane motion between frames than images acquired continuously throughout the cardiac cycle.

Rotational motion caused by LV contraction results in in-plane motion not accounted for by the present registration and warping approach. We have quantified total base-to-apex rotation as 20° in normal examples.^[20] In-plane rotation for an individual slice will be less, and imaging at a single point in the cycle will further reduce the observed rotation.

Images were acquired using inversion rather than saturation pulses to null myocardial signal. Saturation pulses are known to be more sensitive to intra-study changes in heart rate than inversion methods; however, inversion pulses provide better myocardial signal reduction and better contrast between normally and hypo-enhanced regions. The performance of the present technique on saturation-prepared perfusion images was not evaluated.

The presented method for MR perfusion image registration and warping reduced translation and change in observed myocardial area in both short- and long-axis images. It has application to qualitative visual assessment of perfusion defects when images are viewed in cine-loop format and to the generation of quantitative parametric images. The method is fully automated and independent of acquired cardiac orientation.



ACKNOWLEDGMENT

The authors are grateful for financial support by a grant-in-aid from the American Heart Association, Pennsylvania Affiliate #97PAGS27.

REFERENCES

1. Manning, W.J.; Atkinson, D.J.; Grossman, W.; Paulin, S.; Edelman, R.R. First-Pass Nuclear Magnetic Resonance Imaging Studies Using Gadolinium-DTPA in Patients with Coronary Artery Disease. *J. Am. Coll. Cardiol.* **1991**, *18*, 959–965.
2. Rogers, W.J.; Kramer, C.M.; Geskin, G.; Hu, Y.-L.; Theobald, T.M.; Petruolo, S.; Reichek, N. Early Contrast Enhanced MRI Predicts Late Functional Recovery After Reperfused MI. *Circulation* **1999**, *99*, 744–750.
3. Lima, J.A.C.; Judd, R.M.; Bazille, A.; Schulman, S.P.; Atalar, E.; Zerhouni, E.A. Regional Heterogeneity of Human Myocardial Infarcts Demonstrated by Contrast Enhanced MRI: Potential Mechanisms. *Circulation* **1995**, *92*, 1117–1125.
4. Yakota, C.; Nonogi, H.; Miyazaki, S.; Goto, Y.; Maeno, M.; Daikoku, S.; Itoh, A.; Haze, K.; Yamada, N. Gadolinium-Enhanced Magnetic Resonance Imaging in Acute Myocardial Infarction. *Am. J. Cardiol.* **1995**, *75*, 577–581.
5. Rochitte, C.E.; Lima, J.A.; Bluemke, D.A.; Reeder, S.B.; McVeigh, E.R.; Furuta, T.; Becker, L.C.; Melin, J.A. Magnitude and Time Course of Microvascular Obstruction and Tissue Injury After Acute Myocardial Infarction. *Circulation* **1998**, *98* (10), 1006–1014.
6. Cullen, J.H.; Horsfield, M.A.; Reek, C.R.; Cherryman, G.R.; Barnett, D.B.; Samani, N.J. A Myocardial Perfusion Reserve Index in Humans Using First-Pass Contrast-Enhanced Magnetic Resonance Imaging. *J. Am. Coll. Cardiol.* **1999**, *33*, 1386–1394.
7. Machnig, T.; Koroneos, A.; Engles, G.; Bachmann, K.; Simm, C.; Wilke, N.; Ellerman, J.; Zhang, J.; Ya, X.; Merkel, H.; Path, G.; Bache, R.J.; Ugurbil, K. Quantitative Assessment of Myocardial Blood-flow by Ultrafast Magnetic Resonance Imaging. *Z. Kardiol.* **1994**, *83*, 840–850.
8. Vallee, J.P.; Sostman, H.D.; MacFall, J.R.; DeGrado, T.R.; Zhang, J.; Sebbag, L.; Cobb, F.R.; Wheeler, T.; Hedlund, L.W.; Turkington, T.G.; Spritzer, C.E.; Coleman, R.E. Quantification of Myocardial Perfusion by MRI After Coronary Occlusion. *Magn. Reson. Med.* **1998**, *40* (2), 287–297.
9. Yang, G.Z.; Burger, P.; Panting, J.; Gatehouse, P.D.; Rueckert, D.; Pennell, D.J.; Firmin, D.N. Motion and Deformation Tracking for Short-Axis Echo-Planar Myocardial Perfusion Imaging. *Med. Image Anal.* **1998**, *2*, 285–302.
10. Dromigny-Badin, A.; Zhu, Y.M.; Magnin, I.; Revel, D. Fusion of Cine Magnetic Resonance and Contrast-Enhanced First-Pass Magnetic Resonance Data in Patients with Coronary Artery Disease. *Investig. Radiol.* **1998**, *33*, 12–21.
11. Kass, M.; Witkin, A.; Terzopoulos, D. Snakes: Active Contour Models. *Proc. 1st Int. Conf. Comput. Vision* **1987**, 259–268.
12. Ranganath, S. Contour Extraction from Cardiac MRI Studies Using Snakes. *IEEE Trans. Med. Imag.* **1995**, *MI-14*, 328–338.
13. Staib, L.H.; Duncan, J.S. Boundary Finding with Parametrically Deformable Models. *IEEE Trans. Patt. Anal. Machine Intel.* **1992**, *PAMI-14*, 1061–1075.
14. Wu, X.; Murani, S. Image Matching Using a Three Line Scanner. *ISPRS J. Photogrammetry Remote Sens.* **1997**, *52*, 20–32.
15. Fogel, M.A.; Weinberg, P.M.; Chin, A.J.; Fellows, K.E.; Hoffman, E.A. Late Ventricular Geometry and Performance Changes of Functional Single Ventricle Throughout Staged Fontan Reconstruction Assessed by Magnetic Resonance Imaging. *J. Am. Coll. Cardiol.* **1996**, *28*, 212–221.
16. Rogers, W.J.; Kramer, C.M.; Wan, L.; Petruolo, S.; Theobald, T.; Reichek, N. Multiparametric Analysis of MR Myocardial Perfusion Imaging in Normals. *Proc. Int. Magn. Reson. Med.* **1995**, *2*, 877.
17. Becker, D.E.; Can, A.; Turner, J.N.; Tanenbaum, H.L.; Roysam, B. Image Processing Algorithms for Retinal Montage Synthesis, Mapping, and Real-Time Location Determination. *IEEE Trans. Biomed. Eng.* **1998**, *45*, 105–118.
18. Daniais, P.G.; Stuber, M.; Botnar, R.M.; Kissinger, K.V.; Edelman, R.R.; Manning, W.J. Relationship Between Motion of Coronary Arteries and Diaphragm During Free Breathing: Lessons from Real-Time MR Imaging. *AJR Am. J. Roentgenol.* **1999**, *172* (4), 1061–1065.
19. Rogers, W.J.; Shapiro, E.P.; Weiss, J.L.; Buchalter, M.B.; Rademakers, F.E.; Weisfeldt, M.L.; Zerhouni, E.A. Quantification and Correction for Left Ventricular Systolic Long Axis Shortening by Magnetic Resonance Tissue Tagging. *Circulation* **1991**, *84*, 721–731.
20. Buchalter, M.B.; Weiss, J.L.; Rogers, W.J.; Zerhouni, E.A.; Weisfeldt, M.L.; Beyer, R.; Shapiro, E.P. Noninvasive Quantification of Left Ventricular Rotational Deformation in Normal Humans Using Magnetic Resonance Imaging Myocardial Tagging. *Circulation* **1990**, *81*, 1236–1244.

Received November 28, 2001

Accepted May 29, 2002